

## Article

# Proton Transfer in the K-Channel Analog of B-Type Cytochrome *c* Oxidase from *Thermus thermophilus*

Anna Lena Woelke,<sup>1</sup> Anke Wagner,<sup>1</sup> Gegham Galstyan,<sup>1</sup> Tim Meyer,<sup>1</sup> and Ernst-Walter Knapp<sup>1,\*</sup><sup>1</sup>Institute of Chemistry and Biochemistry, Freie Universität Berlin, Berlin, Germany

**ABSTRACT** A key enzyme in aerobic metabolism is cytochrome *c* oxidase (CcO), which catalyzes the reduction of molecular oxygen to water in the mitochondrial and bacterial membranes. Substrate electrons and protons are taken up from different sides of the membrane and protons are pumped across the membrane, thereby generating an electrochemical gradient. The well-studied A-type CcO uses two different entry channels for protons: the D-channel for all pumped and two consumed protons, and the K-channel for the other two consumed protons. In contrast, the B-type CcO uses only a single proton input channel for all consumed and pumped protons. It has the same location as the A-type K-channel (and thus is named the K-channel analog) without sharing any significant sequence homology. In this study, we performed molecular-dynamics simulations and electrostatic calculations to characterize the K-channel analog in terms of its energetic requirements and functionalities. The function of Glu-15B as a proton sink at the channel entrance is demonstrated by its rotational movement out of the channel when it is deprotonated and by its high pK<sub>A</sub> value when it points inside the channel. Tyr-244 in the middle of the channel is identified as the valve that ensures unidirectional proton transfer, as it moves inside the hydrogen-bond gap of the K-channel analog only while being deprotonated. The electrostatic energy landscape was calculated for all proton-transfer steps in the K-channel analog, which functions via proton-hole transfer. Overall, the K-channel analog has a very stable geometry without large energy barriers.

## INTRODUCTION

A key element of aerobic metabolism is the enzyme cytochrome *c* oxidase (CcO), which catalyzes the reduction of molecular oxygen to water. Four electrons and four protons are transferred onto a single oxygen molecule in a stepwise reaction. The integral membrane protein CcO utilizes the resultant energy to pump protons across the membrane, thereby establishing an electrochemical gradient.

The CcO family may be divided into A, B, and C types. The well-studied A-type CcO is most abundant and constitutively expressed in mitochondria and several bacteria (1,2), whereas B- and C-type CcO are expressed in some specialized bacteria under low-oxygen conditions (3). Whereas the C-type CcO is more distant to the others (4), the A and B types share higher sequence similarity and have almost identical compositions of cofactors used for electron transport and enzymatic reaction (5,6). At the positively charged P side of the membrane, CcO takes up electrons from soluble cytochrome *c*. They are transported via the bimetallic copper A center (Cu<sub>A</sub>) to heme a (A type) or heme b (B type), and finally to the binuclear center (BNC), where the chemical reaction takes place. The BNC is composed of heme a<sub>3</sub> and the copper B center (Cu<sub>B</sub>), and has a nearly identical three-dimensional structure in both A- and B-type CcO (5,6). The proton-pumping effi-

ciency differs between the A- and B-type CcO (1 H<sup>+</sup><sub>pump</sub>/e<sup>-</sup> and 0.5 H<sup>+</sup><sub>pump</sub>/e<sup>-</sup>, respectively) (7), although it was speculated that the B-type pump efficiency may be underestimated due to experimental limitations (8). The intermediate states of the catalytic cycle in A-type CcO, which have been investigated intensively (2,9), may differ from those in the B type (10). Also, the proton input pathways of A- and B-type CcO differ from each other. All protons are taken up from the negatively charged N side of the membrane and can be differentiated into chemical protons that are consumed in the reaction and pumped protons, which are pumped across the membrane. In the A-type CcO, the protons are conducted via two different pathways (1,2): 1), the D-channel leading from aspartate (Asp-132, *R. sphaeroides* numbering) at the entrance to glutamate (Glu-286) situated between the hemes; and 2), the K-channel containing lysine (Lys-362) and terminating at tyrosine (Tyr-288), which is covalently bound to His-284 ligating Cu<sub>B</sub>. For the A-type CcO, it is well established that all pumped protons are taken up via the D-channel, and that two chemical protons enter via the D-channel and two enter via the K-channel. In contrast, the B-type CcO was shown to transport all chemical and pumped protons via the same input channel (11), which is located at a similar position as the K-channel of the A-type CcO (6) without sharing significant sequence homology. This K-channel analog in B-type CcO (Fig. 1) involves a hydrogen bond (H-bond) chain of threonines, tyrosines, and serine, and a water molecule with only one

Submitted June 30, 2014, and accepted for publication September 11, 2014.

\*Correspondence: knapp@chemie.fu-berlin.de

Editor: Carmen Domene.

© 2014 by the Biophysical Society  
0006-3495/14/11/2177/8 \$2.00



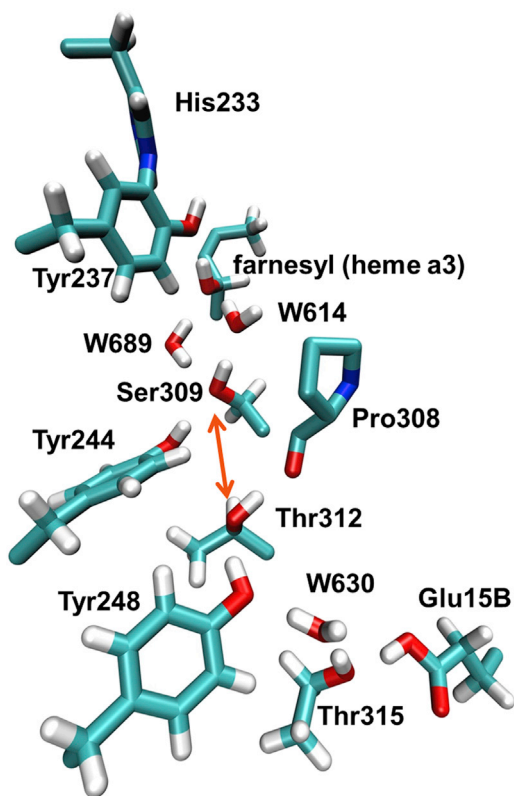


FIGURE 1 Proton wire in the K-channel analog in CcO of *T. thermophilus*. The channel runs from Glu-15B to Tyr-237, with one gap of 4.9 Å in the H-bond chain between Thr-312 and Ser-309 (indicated by an orange arrow). For proton transport, a proton hole is presumably transported from Tyr-237 to Glu-15B via farnesyl, W614, Ser-309, Tyr-244, Thr-312, Tyr-248, W630, and Thr-315. Coordinates were taken from crystal structure PDB 3S8F (6) and hydrogen atoms were added with CHARMM (19). In addition to the channel residues, Pro-308 is depicted (without hydrogens) because its backbone CO group accepts an H-bond from Thr-312, and His-233 is depicted because it is covalently bound to Tyr-237. For clarity, the farnesyl chain of heme  $a_3$  is shown only partially. To see this figure in color, go online.

4.9 Å gap in between Thr-312 and Ser-309 (Fig. 1). Only glutamate and tyrosine at the entrance and terminus, respectively, are conserved among the K-channels of A- and B-type CcO.

For the A-type CcO, the properties of the D-channel for collecting and gating protons have been discussed extensively (12–14), and recently we also found a gating element in the K-channel (15). In the B-type CcO, these functionalities must be accomplished by a single proton input channel that ensures rapid unidirectional proton flow and translocation of pumped protons.

In this study, we use molecular-dynamics (MD) simulations and electrostatic energy computations to explore the energy landscape of proton transfer via the K-channel analog in the B-type CcO. We highlight the key functionalities of specific molecular geometries and offer an explanation for how the channel may ensure proton transport that is rapid as well as unidirectional.

## MATERIALS AND METHODS

### Preparing and performing MD simulations of CcO

The coordinates of subunits I, II, and IIa of CcO from *Thermus thermophilus* were taken from the Protein Data Bank (16) (PDB ID: 3S8F (5)), embedded in a lipid bilayer of phosphatidylcholines modeled with the plug-in of VMD (17), and solvated in a TIP3P (18) water box applying periodic boundary conditions (dimensions: 100 Å × 100 Å × 107.8 Å). We employed the CHARMM22 force field (19), CHARMM36 extension for lipids (20), and in-house-determined parameters for the cofactors (13). The same setup of MD simulation was used previously for the A-type CcO (13). The MD simulations were performed with the software NAMD (21) using a 2 fs time step with SHAKE to fix the bond lengths involving hydrogen atoms and Langevin dynamics with friction constant  $\beta = 1 \text{ ps}^{-1}$  at 300 K temperature. The MD simulations were performed with a flexible cell size and constant ratio of 1:1 for the  $x$  and  $y$  dimensions to stabilize the membrane, which was placed in the  $x$ - $y$  plane. All MD simulations (listed in Table 1) exhibited stable geometries for 100 ns, with root mean-square deviation (RMSD) values for the backbone atoms essentially below 1.2 Å (Fig. S1 in the Supporting Material) and all-atom RMSD values essentially below 1.5 Å (Fig. S2).

### Atomic partial charges of CcO cofactors

We calculated the atomic partial charges of the cofactors as described by Woelke et al. (13), using the quantum-chemical program Jaguar v.7.7 (Schrödinger, LLC, New York, NY) and the B3LYP DFT functional with the LACVP\*\* basis set. First, the cofactor geometries were optimized quantum chemically. All hydrogen atoms were geometry optimized without constraints, whereas the coordinates of nonhydrogen atoms were optimized with respect to bond lengths and bond angles, keeping the corresponding torsion angles fixed. We then computed the electrostatic potentials in the vicinity of the cofactors based on the electronic wave functions and charges of the nuclei, using the same procedure we employed for geometry optimization. We determined the atomic partial charges from the electrostatic potentials of the cofactors by employing a two-stage restraint-electrostatic-potential (RESP) (22,23) procedure. The only difference between our approach and the procedure described by Woelke et al. (13) is that to compute the atomic partial charges of the  $\text{Cu}_B$  center, we included Tyr-237 covalently bound to His-233. The coordinates and atomic partial charges are given in Table S2.

### Computation of $\text{pK}_A$ values and electrostatic energies

We investigated the protonation states in equilibrium of all CcO residues based on preliminary  $\text{pK}_A$  computations (24,25) using just a single structure with optimized hydrogen atom positions based on the crystal structure from *T. thermophilus* with the highest resolution of 1.8 Å (6). The histidine

TABLE 1 MD simulations performed in this work

MD simulation	Redox and protonation state of BNC	Specific protonation in channel
1	$\text{Fe(IV)=O/Cu}_B(\text{II})\text{-OH/Tyr-237-O}^-$	all channel residues protonated (except Tyr-237)
2	$\text{Fe(IV)=O/Cu}_B(\text{II})\text{-OH/Tyr-237-OH}$	all channel residues protonated
3	$\text{Fe(IV)=O/Cu}_B(\text{II})\text{-OH/Tyr-237-O}^-$	deprotonated Tyr-244
4	$\text{Fe(IV)=O/Cu}_B(\text{II})\text{-OH/Tyr-237-OH}$	deprotonated Tyr-244
5	$\text{Fe(IV)=O/Cu}_B(\text{II})\text{-OH/Tyr-237-O}^-$	deprotonated Glu-15B
6	$\text{Fe(IV)=O/Cu}_B(\text{II})\text{-OH/Tyr-237-OH}$	deprotonated Glu-15B

protonations (involving 18 His) are given in Table S1. All other titratable groups (Asp, Glu, Arg, and Lys) are charged, with the following exceptions: the charge-neutral Glu-15B at the entrance of the K-channel analog (discussed in the next section) and the charge-neutral Glu-203, Glu-131B, and Asp-372, which might be involved in proton pumping, but were not analyzed in this study because they are far from the K-channel analog.

To calculate the energy landscape of the proton transfer pathway via the K-channel analog, we used the crystal structure PDB 3S8F (6) embedded in a membrane as described above. The BNC ligands were modeled as described in Woelke et al. (13). We added hydrogen atoms and adjusted the geometry of OH groups of water and side chains (tyrosine and serine) to the different protonation states that potentially can occur during proton transport in the K-channel analog. This modeling also involved adjusting the Tyr-244 side chain for the Tyr-244–Thr-312 switch mechanism (explained in the Results and Discussion section), followed by constrained energy minimization of the modeled region. The  $pK_A$  values were calculated using karlsberg+ (24,25). Crystal water molecules were removed (except for the three crystal water molecules inside the K-channel analog (W614, W630, and W689), which were kept) and a dielectric continuum with  $\epsilon = 80$  was placed in the resulting cavities. Lipid molecules of the membrane with atoms within a 20 Å sphere around the center of the K-channel analog were kept. All other lipids were deleted. We tested this procedure and found it to be appropriate (15). A dielectric continuum with  $\epsilon = 80$  was placed outside of the volume of all atoms (from protein, lipids, and water molecules) that were kept explicitly, whereas inside the volume of explicit atoms,  $\epsilon = 4$ . The moderate value of the dielectric constant of  $\epsilon = 4$  inside the volume of explicit atoms accounts implicitly for a limited variation of atom positions, which is not considered explicitly when only the crystal structure is used to evaluate electrostatic energies. Since the electrostatic continuum implicitly accounts for conformational variability, the computed electrostatic energies also contain entropy contributions from the protein and solvent.

For each of the titratable residues involved in proton translocation inside the channel (Tyr-237, farnesyl<sub>hemea3</sub>, W614, Ser-309, Tyr-244, Thr-312, Tyr-248, W630, Thr-315, and Glu-15B), a structure was modeled for the corresponding deprotonated state. For each of these structures, the  $pK_A$  values and thus the protonation energies of the corresponding residue were calculated with karlsberg+ (24,25). To account for structural changes due to the modeling, the electrostatic contribution to the conformational energy was added to the protonation energy. All of these energy terms were calculated by numerically solving the linearized Poisson-Boltzmann equation using the program APBS (26). To obtain reliable results, the finest grid spacing of 0.25 Å was used.

## Role of electrostatic energy in characterizing proton transfer energetics

A precise evaluation of proton transfer energetics requires a consideration of the free energy, which is computationally difficult to assess. Usually, it requires MD simulations beyond the microsecond time regime and is subject to the uncertainties of the employed energy function, which for such long simulation times may drive the molecular system into unphysical conformational regimes. The free energy combines the influence of enthalpy and entropy. Whereas entropy is only indirectly accessible by the conformational variability, enthalpy relies on the interplay between kinetic and potential energies. Based on the second virial theorem (27), the average kinetic energy is proportional to the number of degrees of freedom of the molecular system and therefore does not change in a proton transfer process.

The enthalpy consists of bonded (covalent) and nonbonded (van der Waals (vdW) and Coulomb) energies. A critical part of the bonded energy is the contribution of the transferred proton that is covalently bound to different molecular groups before and after the transfer step. However, we showed that *ab initio* computations of  $pK_A$  values using a combination of high-precision quantum-chemical and electrostatic energy evaluations

yield an RMSD to corresponding measured values of 0.5 pH units (28). This agreement demonstrates that the thermodynamic averages of 1), non-electrostatic quantum-chemical contributions to  $pK_A$  values do not depend on the environment; 2), vdW interactions are practically identical before and after a change in protonation; and 3), covalent interactions inside other not directly covalently connected molecular groups (of the solute) that are spectators in the considered proton transfer step also do not change. Further support for these conclusions comes from extensive evaluations of  $pK_A$  values of titratable groups in proteins based on the measured  $pK_A$  values in solution (24). These  $pK_A$  values are transformed by electrostatic energy computations to the corresponding protein environment with an RMSD to measured values of 1.1 pH units. Hence, it is justifiable to consider only electrostatic energies to characterize proton transfer processes, since they make the main contribution to the energetics of such processes.

Another reason to consider only the electrostatic energies is the fact that our computations are based on crystal structures. This may yield arbitrary contributions for covalent and vdW interactions, since these interactions are very sensitive to small variations of 0.1 Å in atomic coordinates for individual conformations, whereas electrostatic energies with their very mild  $1/r$  distance dependence are relatively insensitive to such small changes. Although the electrostatic energies computed in this study refer to a single conformation, they implicitly consider many conformations by using a dielectric continuum for the solvent and the protein. Thus, they also account for entropy contributions as noted above.

## RESULTS AND DISCUSSION

### Investigation of the K-channel analog

After oxygen splitting occurs, the first proton is likely taken up in the  $P_R$  state (29), which is characterized by an access electron inside the BNC that is composed of Fe(IV)=O/Cu(II)-OH/Tyr-237-O<sup>-</sup>. The K-channel analog, as depicted in Fig. 1, starts with Glu-15B at the N side of the membrane and terminates at Tyr-237. As has been shown by quantum-chemical calculations (30), the proton wire in the channel is composed of several H-bonded OH groups that are protonated in the resting state and conduct protons via a proton-hole transfer mechanism. We performed MD simulations to investigate the conformational stability or mobility of residues in the K-channel analog in different protonation states. A 100 ns MD simulation was performed with all three subunits of CcO embedded in a phospholipid membrane, as described in Materials and Methods, with the BNC modeled in the  $P_R$  state (Table 1, simulation No. 1). In the  $P_R$  state (Table 1, No. 1), the K-channel analog exhibits a very stable geometry for the full MD simulation time, as evidenced, for example, by the low RMSD value of 0.8 Å of the K-channel analog residues (alignment on all backbone atoms and RMSD measurement on all atoms of channel residues; Fig. S3). All H-bonds from Glu-15B to the deprotonated Tyr-237 are pointing toward the BNC fluctuating around an oxygen-oxygen distance of 2.8 Å corresponding to ideal H-bond geometry (Fig. S4 A). Tyr-244 donates an H-bond to Ser-309, whereas Thr-312 donates its H-bond to the backbone oxygen of Pro-308 (see Fig. 1), thus leaving a gap of ~5 Å in the H-bond chain, which is not bridged by a water molecule throughout the simulation (see further discussion below). The crystal water molecule W614 moves from

downward of the Tyr-237 oxygen to upward, but remains H-bonded to the negatively charged Tyr-237 side chain. The other two crystal waters inside the K-channel analog, W630 and W689, remain at their positions during the whole MD simulation time of 100 ns. This rigid channel geometry may be essential for function in the high-temperature environment in which *T. thermophilus* resides.

The MD simulation with protonated Tyr-237 (Table 1, No. 2) exhibits a geometry similar to that observed in the simulation with deprotonated Tyr-237, but some H-bonds of the K-channel analog are slightly less stable (see Fig. S4 B). Tyr-237 loses its H-bond contact to the OH group of farnesyl from heme  $a_3$ , and also the H-bond between Ser-309 and Tyr-244 is split, but bridged by a water molecule.

### The proton-hole sink: Glu-15B

The entrance of the K-channel analog consists of the glutamate residue Glu-15B, which is conserved among channels of A- and B-type CcO (5,6,31,32). We performed MD simulations with protonated (Table 1, No. 2) and deprotonated (Table 1, No. 6) Glu-15B, and found that the protonated Glu-15B forms a stable H-bond toward Thr-315 with an average distance of 2.8 Å (Fig. S4, A and B) over 100 ns (Fig. 2 A), whereas the deprotonated Glu-15B does not (Fig. S5, A and B). The deprotonated Glu-15B first accepts an H-bond from Thr-315 (Fig. 2 B), but loses this contact after 10.8 ns or 1.4 ns MD simulation with protonated Tyr-237 or deprotonated Tyr-237, respectively. The deprotonated Glu-15B swings out of the hydrophobic channel entrance toward bulk water, as has also been demonstrated by quantum-chemical calculations (30,33), and does not return in the deprotonated state (Fig. S5, A and B). As soon as Glu-15B loses contact to Thr-315, the H-bonds of the proton wire of the K-channel analog (see Fig. 1) turn inward, pointing with the hydrogen atoms toward the BNC (Fig. 2 C). After a >40 ns simulation with deprotonated Glu-15B, the water molecule W630 leaves the channel toward bulk water without returning (Fig. S5, A and B). This creates a gap between Thr-315 and Tyr-248, which slightly destabilizes the H-bond chain in the K-channel analog.

In the crystal structure PDB 3S8F (6), Glu-15B is pointing toward Thr-315 (see Fig. 1) and may either be protonated and donate an H-bond to Thr-315 or be deprotonated and accept an H-bond. Preliminary  $pK_A$  computations based solely on the crystal structure yield a  $pK_A$  value for Glu-15B of 6.8. However, in MD simulations, the deprotonated Glu-15B moves out of the K-channel analog toward bulk water and the protonated Glu-15B remains precisely at the crystal structure position. Thus, we conclude that Glu-15B is protonated in the 3S8F structure (6). Interestingly, the other crystal structures of CcO from *T. thermophilus* exhibit a Glu-15B position more distant from Thr-315 (3.41 Å in PDB 1EHK (34) and 3.64 Å in PDB 1XME (35)) and the mean B factor of the Glu-15B side chain atoms is 41.8 Å<sup>2</sup>

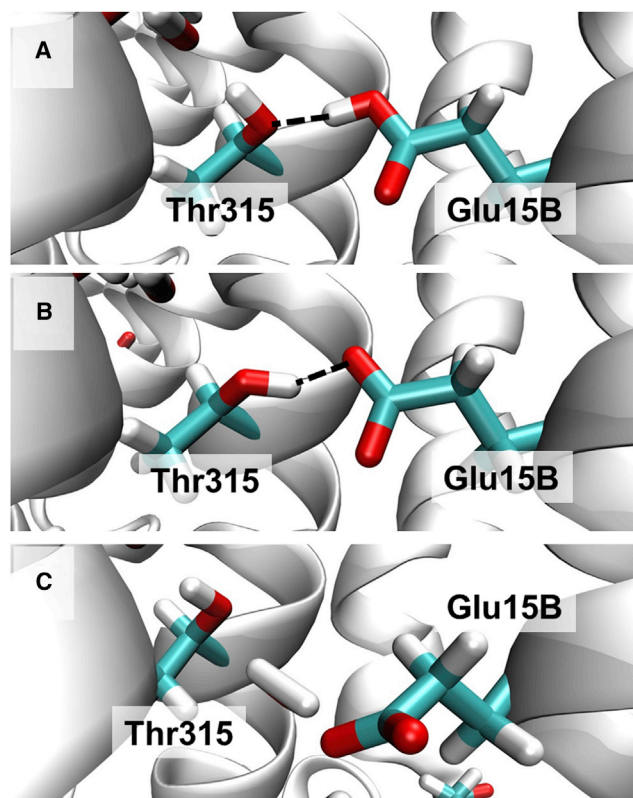


FIGURE 2 Different positions of Glu-15B depending on the protonation state. (A) The crystal structure (PDB ID: 3S8F (6)) with protonated Glu-15B donating an H-bond to Thr-315. The MD simulation with protonated Glu-15B remains close to this position. (B) After energy minimization, deprotonated Glu-15B accepts an H-bond from Thr-315. (C) Snapshot of the MD simulation after 15.0 ns. Glu-15B moves out of the K-channel analog toward bulk water and loses connectivity to Thr-315, which then forms an H-bond inward with the hydrogen atom pointing to the BNC and remains there for the rest of the 100 ns MD simulation. H-bonds are indicated by dashed lines. To see this figure in color, go online.

larger than the mean B factor (26.1 Å<sup>2</sup>) of the side-chain atoms of the other K-channel analog residues in the crystal structure 3S8F (6) (similar relations hold for the other crystal structures). This suggests that Glu-15B is more flexible and may occasionally move from its main conformation, where it is protonated and points inward to a second conformation that is deprotonated and points to bulk water.

In summary, Glu-15B of the K-channel analog is likely protonated and donates an H-bond to Thr-315 in the resting state of the channel, where CcO is ready to take up a new electron. However, Glu-15B may easily donate its proton, become deprotonated, and move out toward the channel entrance in bulk water, where it may transiently accept a new proton. This behavior of Glu-15B renders it an excellent sink for proton holes, promoting rapid proton uptake by CcO.

### Tyr-244, the valve

In the crystal structure obtained by Tiefenbrunn et al. (6), the only gap in the H-bond chain of the K-channel analog

is between Thr-312 and Ser-309, which are 4.9 Å apart (oxygen-oxygen distance; Fig. 1). This gap could be bridged either by Tyr-244 swinging toward Thr-312 or by one additional water molecule, as suggested previously (11). However, after carefully inspecting the latest crystal structure at 1.8 Å resolution, Tiefenbrunn et al. (6) did not observe an electron density that could correspond to a water molecule bridging this gap. Furthermore, the Tyr-244 position is virtually identical in all available crystal structures and has a low B factor throughout (6,34,35). Likewise, all of our modeling attempts to move Tyr-244 or place an additional water molecule inside this gap did not lead to a stable conformation in MD simulations (data not shown). Instead, we observed a switching mechanism of Tyr-244.

Whereas the protonated Tyr-244 remained at the crystal structure position during the whole 100 ns MD simulation (Fig. 3 A; Table 1, No. 2; H-bond distances in Fig. S6, A and B), the deprotonated Tyr-244 immediately moved between Ser-309 and Thr-312, accepting H-bonds from both of them (Fig. 3 B; Table 1, No. 3; H-bond distances in Fig. S6, A and B). This geometry was stable for only 0.3 ns, and then a water molecule that was placed inside the protein during solvation moved between Tyr-244 and Ser-309, such that they were still H-bond connected (Fig. and H-bond distances in Fig. S6, A and B). The other H-bond between Thr-312 and Tyr-244 remained stable for practically the whole 100 ns simulation, with an average distance of 2.8 Å (Fig. 3 C and H-bond distances in Fig. S6, A and B).

In conclusion, the gap between Ser-309 and Thr-312 is only bridged by Tyr-244 after its deprotonation. This behavior renders the Tyr-244–Thr-312 pair an optimal switch, ensuring unidirectional proton transport. In the resting state of the channel, where CcO is ready to take up a new electron, Tyr-244 is only H-bonded with the upstream Ser-309 close to the BNC, whereas Thr-312 donates an H-bond to the Pro-308 backbone oxygen atom, which has no hydrogen atom that could potentially leak toward the channel entrance. Only after Tyr-244 has donated its proton toward the BNC does the Tyr-244–Thr-312 switch make the K-channel analog proton conducting again. The deprotonated Tyr-244 may quickly obtain a new proton from Glu-

15B at the channel entrance, which converts the protonation of the K-channel analog back to the resting state of the channel. Thus, the K-channel analog does not function solely via a simple Grotthuss proton conductor consisting of a single wire of connected H-bonds (36), as suggested previously (11,30); rather, it is a two-wire Grotthuss conductor interrupted by Tyr-244, which if deprotonated makes a conformational change to connect the two wires transiently.

We also calculated the so-called action  $pK_A$  of Tyr-244, assuming that a (nonequilibrium) proton hole is localized at Tyr-244. Such action  $pK_A$  values describe the local electrostatic energies within the reaction sequence of proton-hole transfer inside the K-channel analog. The alternative  $pK_A$  of Tyr-244 in equilibrium with solvent pH is not useful for our question of interest because it depends on the changes in protonation pattern of all other titratable residues and the corresponding conformational change of the protein. However, these changes do not reflect the physiological conditions of the proton-transfer reaction. The action  $pK_A$  for Tyr-244 is 7.0 in a conformation corresponding to the crystal structure involving only one H-bond with Ser-309. However, this value drops to 2.8 with the conformational change of Tyr-244 accepting two H-bonds from Ser-309 and Thr-312. This clearly demonstrates that the deprotonated Tyr-244 needs to be stabilized by an additional H-bond from Thr-312, whereas the protonated Tyr-244 is in a more stable conformation when it donates only one H-bond to Ser-309, as observed in the crystal structure.

The Tyr-244–Thr-312 switch is supported by experimental data. The Thr312Val mutant was shown to have more severe effects on CcO function than other channel mutants, such as Tyr248Phe and Thr315Val, which strongly reduced or even abolished enzymatic activity in experiments (11,37,38). In a study by Smirnova et al. (39), the Thr312Val and Tyr244Phe mutants of CcO were able to take up the first proton after oxygen splitting, but the efficiency of the second proton uptake was significantly reduced. The authors concluded that these mutations interfere with structural changes that are rate limiting for the second proton transfer (39). In this study, we have demonstrated that the suggested structural change is connected to the ability of Tyr-244 to

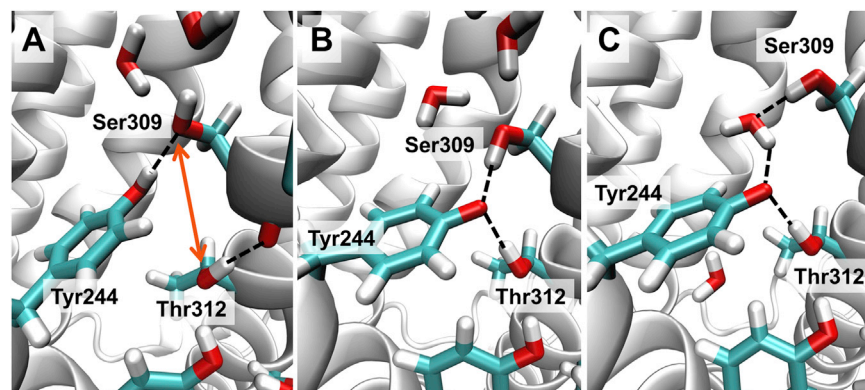


FIGURE 3 Different positions of Tyr-244 depending on its protonation state. (A) The crystal structure (PDB ID: 3S8F (6)) with protonated Tyr-244. The 4.9 Å gap between Thr-312 and Ser-309 is indicated by an orange arrow. During the MD simulation with Tyr-244 protonated (Table 1, No. 2), it remains close to the position in the crystal structure. (B) Snapshot of the MD simulation with deprotonated Tyr-244 (Table 1, No. 4) after 50 ps. The deprotonated Tyr-244 moves into the Thr-312–Ser-309 gap immediately. H-bonds are indicated by dashed lines. (C) Snapshot of the MD simulation with deprotonated Tyr-244 (Table 1, No. 4) after 17.6 ns. One water molecule moves in between Ser-309 and Tyr-244.

move and fulfill its switching function in the K-channel analog, thereby controlling proton conductance.

### Tyr-237: the branching point

The K-channel analog terminates at Tyr-237, which is covalently bound to one of the Cu<sub>B</sub>-ligating histidines and is conserved in all types of CcO (4–6). It takes part in the enzymatic reaction of CcO by donating a proton as well as an electron in the oxygen-splitting reaction, thus forming a tyrosyl radical. In the catalytic cycle, this Tyr-237 radical receives a new electron and a new proton in separate steps. In this study, we investigated the P<sub>R</sub> state, in which Tyr-237 has received an electron but not yet a proton. Interestingly, the F state could not be observed spectroscopically in the B-type CcO (29,40), perhaps because in the B-type CcO, the Tyr-237 receives the first chemical proton (41) instead of the Cu<sub>B</sub>-ligating hydroxyl as in A-type CcO. The state after this proton is received in the B-type CcO may be the F state or an intermediate before F-state formation.

We also performed MD simulations with protonated (Table 1, No. 2) and deprotonated (Table 1, No. 1) Tyr-237 (Fig. 4). In both MD simulations, the H-bond network of the K-channel analog is very stable. For deprotonated Tyr-237 (Table 1, No. 1), all H-bonds of the K-channel analog point inward to the BNC, whereas the crystal water W614 moves slightly above Tyr-237 but remains H-bonded with it (H-bond distances in Fig. S4 A). For the protonated Tyr-237 (Table 1, No. 2), the H-bonds of the proton wire in the upper part of the channel point down toward the N side, but in the lower part of the channel from Thr-312 to Glu-15B, the H-bonds still point inward to the BNC (H-bond distances in Fig. S4 B). This underlines the function of the Tyr-244–Thr-312 switch, because this geometry is not prone to proton leakage from Tyr-237 to the N side of the K-channel analog.

The oxygen atom of Tyr-237 is located at a distance of 5.0 Å from the oxygen ligand of heme a<sub>3</sub> (6) (Fig. 4) and

may donate chemical protons to this oxygen, probably via one or two water molecules (a suggested pathway is indicated in Fig. 4), which are not present in the crystal structure and thus may occupy their positions only transiently. Tyr-237 is the residue that terminates the proton input channel at the BNC. Since there is only one proton input channel in B-type CcO, it is suggestive that also the pumped protons are transferred via Tyr-237. No alternative pathway for proton transfer from the K-channel analog to the putative proton loading site (PLS) is visible in the CcO crystal structure (Fig. 4). Between Tyr-237 and the putative PLS, which was proposed to be around the propionates of heme a<sub>3</sub> (42,43), the only titratable groups are the Cu<sub>B</sub> ligands and Thr-302 (Fig. 4). The surroundings of Tyr-237 involve several hydrophobic residues, which are not suitable for proton transfer. Therefore, Tyr-237 may likely be the branching point at which the routes of chemical and pumped protons diverge (suggested pathways are indicated in Fig. 4). A function analog to Tyr-237 is accomplished by Glu-286 in the D-channel of A-type CcO (2) (*R. sphaeroides* numbering).

The approximate location of the pathways for chemical and pumped protons beyond Tyr-237 is indicated in Fig. 4. However, the mechanism underlying how chemical and pumped protons are differentiated beyond Tyr-237 needs further investigation. Proton movement is controlled by electrons entering the BNC and, most likely, chemical protons are dragged from Tyr-237 into the BNC by a low pK<sub>A</sub> of the oxygen ligand at heme a<sub>3</sub> and pumped protons are dragged by a low pK<sub>A</sub> of the PLS. From the crystal structure with modeled hydrogens, we computed a pK<sub>A</sub> of 12.8 for Tyr-237 in the P<sub>R</sub> state based on electrostatic calculations. However, as Tyr-237 is covalently bound to the Cu<sub>B</sub>-ligating histidine, its pK<sub>A</sub> will be strongly influenced by the redox-state of Cu<sub>B</sub> and refinement of the pK<sub>A</sub> computation using quantum-mechanical calculations will be needed.

The actual protonation state of Tyr-237 in the crystal structure (PDB ID: 3S8F (6)) cannot be determined with

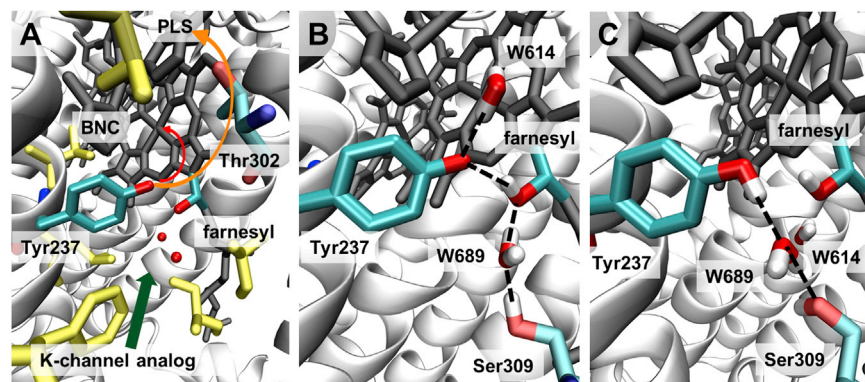


FIGURE 4 Different positions of Tyr-237 depending on its protonation state. (A) The crystal structure (PDB ID: 3S8F (6)) with the environment of Tyr-237. Tyr-237 at the end of the K-channel analog (green arrow) is close to or even part of the BNC (black stick model) and at a 5.0 Å distance from the OH group of farnesyl from heme a<sub>3</sub>. The putative PLS is above the BNC, with a few hydrophilic residues (e.g., Thr-302) in between. Hydrophobic residues around Tyr-237 are shown in yellow. The putative pathways of the chemical (red) and pumped (orange) protons above Tyr-237 are indicated by arrows, but the exact locations of the proton pathways are not known. (B) Typical snapshot of MD simulation with deprotonated Tyr-237 (Table 1, No. 1) at 47.0 ns. The deprotonated Tyr-237 remains at the crystal structure position with a stable H-bond from farnesyl of heme a<sub>3</sub> (O-O distance 2.6 Å). The crystal water W614 moves above Tyr-237 and forms a stable H-bond (O-O distance 2.8 Å). H-bonds are indicated by dashed lines. Nonpolar hydrogens are not shown. (C) Typical snapshot of MD simulation with protonated Tyr-237 (Table 1, No. 2) at 64.0 ns. The H-bond between Tyr-237 and farnesyl of heme a<sub>3</sub> is shown, and the water molecule W614 bridges Tyr-237 and Ser-309 (the O-O distances of Tyr-237 and Ser-309 with W614 are 2.8 Å and 2.6 Å, respectively).

Tyr-237 remains at the crystal structure position with a stable H-bond from farnesyl of heme a<sub>3</sub> (O-O distance 2.6 Å). The crystal water W614 moves above Tyr-237 and forms a stable H-bond (O-O distance 2.8 Å). H-bonds are indicated by dashed lines. Nonpolar hydrogens are not shown. (C) Typical snapshot of MD simulation with protonated Tyr-237 (Table 1, No. 2) at 64.0 ns. The H-bond between Tyr-237 and farnesyl of heme a<sub>3</sub> is shown, and the water molecule W614 bridges Tyr-237 and Ser-309 (the O-O distances of Tyr-237 and Ser-309 with W614 are 2.8 Å and 2.6 Å, respectively).

certainty. Still, two arguments point to a protonated Tyr-237: 1), the average geometry from MD simulation with a protonated Tyr-237 deviates the least from the crystal structure geometry, and even crystal water molecules around Tyr-237 remain at their position; and 2), if Tiefenbrunn et al.'s (6) conclusion about a peroxide in the BNC is correct, Tyr-237 would be in the state right before donating a proton.

### Proton transfer energy landscape

To demonstrate how the K-channel analog might operate, we calculated the electrostatic contribution of the energy differences of all steps of proton transport using our software karlsberg+ (24,25). However, these energy barriers are only approximate because we used the crystal structure (6) for our calculations and adjusted only the BNC ligands to the corresponding redox state with split dioxygen (see Table 1), added hydrogen atoms, made small geometric adjustments of the OH groups for the different protonation states, and modeled the conformational change of Tyr-244 for the Thr-312–Tyr-244 switch. The proton-transfer sequence starts in the P<sub>R</sub> state with a deprotonated Tyr-237 and all other residues involved in K-channel proton transport in their neutral-charge state. As can be seen in Fig. 5, almost all proton-transfer steps exhibit a favorable electrostatic energy relative to the proton hole at the starting point at Tyr-237. The most unfavorable energy is observed for the crystal water W630 forming a hydroxyl ion, which is due to the high general pK<sub>A</sub> value of water in solution (pK<sub>A</sub> = 15.75). However, another reason for the large activation barrier could be the uncertainty of the oxygen atom position of W630, which is taken from the CcO crystal structure and may differ under physiological conditions in the proton-transfer reaction.

Our results demonstrate the feasibility of the Tyr-244–Thr-312 switch, since deprotonation of Tyr-244 is energetically

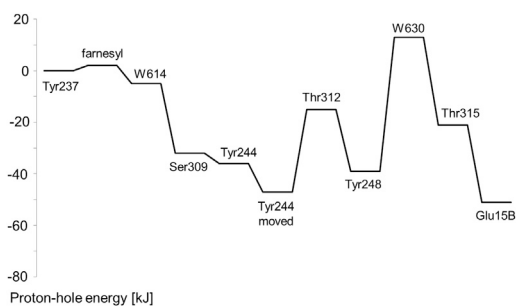


FIGURE 5 Electrostatic energy landscape of the proton hole inside the K-channel analog. Electrostatic energies for all deprotonation steps were calculated using the software karlsberg+ (24,25) as described in Materials and Methods. Transport of a proton hole along the K-channel analog starts at Tyr-237, which is deprotonated and donates its proton to the BNC. The proton hole subsequently moves along a linear chain of deprotonatable residues until it reaches Glu-15B. After deprotonation of Tyr-244, this residue moves inside the gap between Ser-309 and Thr-312. The electrostatic energies before and after this conformational change are depicted.

favorable when it accepts one H-bond from Ser-309, but becomes even more favorable when Tyr-244 changes its conformation to form H-bonds with both Ser-309 and Thr-312 (Fig. 5).

In the last step in proton-hole conduction in the K-channel analog, Glu-15B donates its proton with the largest favorable energy. This may ensure that no negative charge accumulates inside the proton channel that could lead to proton leakage through the channel. The deprotonated Glu-15B then swings out toward bulk water and receives a new proton to fulfill its function to serve as proton-hole sink at the channel entrance.

### CONCLUSIONS

In this study, we analyzed the properties of the K-channel analog in CcO of *T. thermophilus*. We demonstrated that proton transport via the K-channel analog works smoothly, with no oversized energy barriers, using a proton-hole transport mechanism. We identified two important functionalities: 1), Glu-15B at the channel entrance is a proton-hole sink; and 2), unidirectional proton flow is accomplished by the Tyr-244–Thr-312 switch, where deprotonated Tyr-244 moves inside the gap between Thr-312 and Ser-309. These findings may explain the outcome of several mutational studies and may inform the setup for new experiments. Furthermore, enhanced knowledge about the K-channel analog will provide an important basis for investigating the aberrant pumping properties of B-type as compared with A-type CcO (44).

### SUPPORTING MATERIAL

Six figures, two tables, RMSD values for all simulations, important hydrogen-bond distances, partial charges of cofactors, and the histidine protonation pattern are available at [http://www.biophysj.org/biophysj/supplemental/S0006-3495\(14\)00948-5](http://www.biophysj.org/biophysj/supplemental/S0006-3495(14)00948-5).

The authors thank Dr. Joachim Heberle for fruitful discussions.

This work was supported by the Deutsche Forschungsgemeinschaft within the framework of Collaborative Research Center 1078 (project C2) and the research training group Computational System Biology.

### REFERENCES

1. Brzezinski, P., and R. B. Gennis. 2008. Cytochrome c oxidase: exciting progress and remaining mysteries. *J. Bioenerg. Biomembr.* 40:521–531.
2. Kaila, V. R., M. I. Verkhovsky, and M. Wikström. 2010. Proton-coupled electron transfer in cytochrome oxidase. *Chem. Rev.* 110:7062–7081.
3. Han, H., J. Hemp, ..., R. B. Gennis. 2011. Adaptation of aerobic respiration to low O<sub>2</sub> environments. *Proc. Natl. Acad. Sci. USA.* 108:14109–14114.
4. Buschmann, S., E. Warkentin, ..., H. Michel. 2010. The structure of cbb3 cytochrome oxidase provides insights into proton pumping. *Science.* 329:327–330.
5. Qin, L., C. Hiser, ..., S. Ferguson-Miller. 2006. Identification of conserved lipid/detergent-binding sites in a high-resolution structure

- of the membrane protein cytochrome c oxidase. *Proc. Natl. Acad. Sci. USA*. 103:16117–16122.
6. Tiefenbrunn, T., W. Liu, ..., V. Cherezov. 2011. High resolution structure of the ba3 cytochrome c oxidase from *Thermus thermophilus* in a lipidic environment. *PLoS ONE*. 6:e22348.
  7. von Ballmoos, C., P. Adelroth, ..., P. Brzezinski. 2012. Proton transfer in ba(3) cytochrome c oxidase from *Thermus thermophilus*. *Biochim. Biophys. Acta*. 1817:650–657.
  8. Rauhamäki, V., and M. Wikström. 2014. The causes of reduced proton-pumping efficiency in type B and C respiratory heme-copper oxidases, and in some mutated variants of type A. *Biochim. Biophys. Acta*. 1837:999–1003.
  9. Siegbahn, P. E., and M. R. Blomberg. 2010. Quantum chemical studies of proton-coupled electron transfer in metalloenzymes. *Chem. Rev*. 110:7040–7061.
  10. Siletsky, S. A., I. Belevich, ..., M. I. Verkhovskiy. 2009. Time-resolved OH<sup>-</sup>→EH transition of the aberrant ba3 oxidase from *Thermus thermophilus*. *Biochim. Biophys. Acta*. 1787:201–205.
  11. Chang, H. Y., J. Hemp, ..., R. B. Gennis. 2009. The cytochrome ba3 oxygen reductase from *Thermus thermophilus* uses a single input channel for proton delivery to the active site and for proton pumping. *Proc. Natl. Acad. Sci. USA*. 106:16169–16173.
  12. Kaila, V. R., M. I. Verkhovskiy, ..., M. Wikström. 2008. Glutamic acid 242 is a valve in the proton pump of cytochrome c oxidase. *Proc. Natl. Acad. Sci. USA*. 105:6255–6259.
  13. Woelke, A. L., G. Galstyan, ..., E. W. Knapp. 2013. Exploring the possible role of Glu286 in CcO by electrostatic energy computations combined with molecular dynamics. *J. Phys. Chem. B*. 117:12432–12441.
  14. Yang, S., and Q. Cui. 2011. Glu-286 rotation and water wire reorientation are unlikely the gating elements for proton pumping in cytochrome C oxidase. *Biophys. J*. 101:61–69.
  15. Woelke, A. L., G. Galstyan, and E. W. Knapp. 2014. Lysine 362 in Cytochrome c Oxidase Regulates Opening of the K-Channel via Changes in pKa and Conformation. *Biochim. Biophys. Acta*. <http://www.sciencedirect.com/science/article/pii/S0005272814005647>.
  16. Berman, H. M., J. Westbrook, ..., P. E. Bourne. 2000. The Protein Data Bank. *Nucleic Acids Res*. 28:235–242.
  17. Humphrey, W., A. Dalke, and K. Schulten. 1996. VMD: visual molecular dynamics. *J. Mol. Graph*. 14:33–38, 27–28.
  18. Jorgensen, W. L., J. Chandrasekhar, J. D. Madura, R. W. Impey, and M. L. Klein. 1983. Comparison of simple potential functions for simulating liquid water. *J. Chem. Phys*. 79:926.
  19. Brooks, B. R., C. L. Brooks, 3rd, ..., M. Karplus. 2009. CHARMM: the biomolecular simulation program. *J. Comput. Chem*. 30:1545–1614.
  20. Klauda, J. B., R. M. Venable, ..., R. W. Pastor. 2010. Update of the CHARMM all-atom additive force field for lipids: validation on six lipid types. *J. Phys. Chem. B*. 114:7830–7843.
  21. Phillips, J. C., R. Braun, ..., K. Schulten. 2005. Scalable molecular dynamics with NAMD. *J. Comput. Chem*. 26:1781–1802.
  22. Bayly, C. I., P. Cieplak, W. Cornell, and P. A. Kollman. 1993. A well-behaved electrostatic potential based method using charge restraints for deriving atomic charges—the RESP model. *J. Phys. Chem*. 97:10269–10280.
  23. Cornell, W. D., P. Cieplak, C. I. Bayly, and P. A. Kollman. 1993. Application of RESP charges to calculate conformational energies, hydrogen-bond energies, and free-energies of solvation. *J. Am. Chem. Soc*. 115:9620–9631.
  24. Kieseritzky, G., and E. W. Knapp. 2008. Optimizing pKa computation in proteins with pH adapted conformations. *Proteins*. 71:1335–1348.
  25. Rabenstein, B., and E. W. Knapp. 2001. Calculated pH-dependent population and protonation of carbon-monooxy-myoglobin conformers. *Biophys. J*. 80:1141–1150.
  26. Baker, N. A., D. Sept, ..., J. A. McCammon. 2001. Electrostatics of nanosystems: application to microtubules and the ribosome. *Proc. Natl. Acad. Sci. USA*. 98:10037–10041.
  27. Hirschfelder, J. O., F. T. McClure, and I. F. Weeks. 1942. Second virial coefficients and the forces between complex molecules. *J. Chem. Phys*. 10:201.
  28. Schmidt am Busch, M., and E. W. Knapp. 2004. Accurate pKa determination for a heterogeneous group of organic molecules. *ChemPhysChem*. 5:1513–1522.
  29. Smirnova, I. A., D. Zaslavsky, ..., P. Brzezinski. 2008. Electron and proton transfer in the ba(3) oxidase from *Thermus thermophilus*. *J. Bioenerg. Biomembr*. 40:281–287.
  30. Noodleman, L., W. G. Han Du, ..., R. C. Walker. 2014. Linking chemical electron-proton transfer to proton pumping in cytochrome c oxidase: broken-symmetry DFT exploration of intermediates along the catalytic reaction pathway of the iron-copper dinuclear complex. *Inorg. Chem*. 53:6458–6472.
  31. Ostermeier, C., A. Harrenga, ..., H. Michel. 1997. Structure at 2.7 Å resolution of the *Paracoccus denitrificans* two-subunit cytochrome c oxidase complexed with an antibody FV fragment. *Proc. Natl. Acad. Sci. USA*. 94:10547–10553.
  32. Yoshikawa, S., K. Shinzawa-Itoh, ..., T. Tsukihara. 1998. Redox-coupled crystal structural changes in bovine heart cytochrome c oxidase. *Science*. 280:1723–1729.
  33. Fee, J. A., D. A. Case, and L. Noodleman. 2008. Toward a chemical mechanism of proton pumping by the B-type cytochrome c oxidases: application of density functional theory to cytochrome ba3 of *Thermus thermophilus*. *J. Am. Chem. Soc*. 130:15002–15021.
  34. Soulimane, T., G. Buse, ..., M. E. Than. 2000. Structure and mechanism of the aberrant ba(3)-cytochrome c oxidase from *Thermus thermophilus*. *EMBO J*. 19:1766–1776.
  35. Hunsicker-Wang, L. M., R. L. Pacoma, ..., C. D. Stout. 2005. A novel cryoprotection scheme for enhancing the diffraction of crystals of recombinant cytochrome ba3 oxidase from *Thermus thermophilus*. *Acta Crystallogr. D Biol. Crystallogr*. 61:340–343.
  36. Agmon, N. 1995. The Grothuss mechanism. *Chem. Phys. Lett*. 244:456–462.
  37. Chang, H. Y., S. K. Choi, ..., R. B. Gennis. 2012. Exploring the proton pump and exit pathway for pumped protons in cytochrome ba3 from *Thermus thermophilus*. *Proc. Natl. Acad. Sci. USA*. 109:5259–5264.
  38. Smirnova, I., J. Reimann, ..., P. Adelroth. 2010. Functional role of Thr-312 and Thr-315 in the proton-transfer pathway in ba3 Cytochrome c oxidase from *Thermus thermophilus*. *Biochemistry*. 49:7033–7039.
  39. Smirnova, I., H. Y. Chang, ..., P. Brzezinski. 2013. Single mutations that redirect internal proton transfer in the ba3 oxidase from *Thermus thermophilus*. *Biochemistry*. 52:7022–7030.
  40. von Ballmoos, C., R. B. Gennis, ..., P. Brzezinski. 2011. Kinetic design of the respiratory oxidases. *Proc. Natl. Acad. Sci. USA*. 108:11057–11062.
  41. Siletsky, S. A., I. Belevich, ..., M. I. Verkhovskiy. 2007. Time-resolved single-turnover of ba3 oxidase from *Thermus thermophilus*. *Biochim. Biophys. Acta*. 1767:1383–1392.
  42. Blomberg, M. R., and P. E. Siegbahn. 2012. The mechanism for proton pumping in cytochrome c oxidase from an electrostatic and quantum chemical perspective. *Biochim. Biophys. Acta*. 1817:495–505.
  43. Kaila, V. R., V. Sharma, and M. Wikström. 2011. The identity of the transient proton loading site of the proton-pumping mechanism of cytochrome c oxidase. *Biochim. Biophys. Acta*. 1807:80–84.
  44. Lee, H. J., J. Reimann, ..., P. Adelroth. 2012. Functional proton transfer pathways in the heme-copper oxidase superfamily. *Biochim. Biophys. Acta*. 1817:537–544.



# Supporting Information

## Proton Transfer in the K-Channel Analogue of B-Type Cytochrome *c* Oxidase from *Thermus thermophilus*

Anna Lena Woelke, Anke Wagner, Gegham Galstyan, Tim Meyer, Ernst-Walter Knapp\*

Institute of Chemistry and Biochemistry, Freie Universität Berlin, D-14195 Berlin, Germany

\* corresponding author: E W Knapp, knapp@chemie.fu-berlin.de

### Table of content:

Figure S1: RMSD of CcO backbone atoms	S2
Figure S2: RMSD of CcO of all protein atoms	S2
Figure S3: RMSD of CcO of K-channel analogue residues	S3
Figure S4: Hydrogen-bonding distances between polar oxygen atoms in the K-channel analogue	S4
Figure S5: Hydrogen-bonding distances between polar oxygen atoms at the entrance of the K-channel analogue	S5
Figure S6: Hydrogen-bonding distances between polar oxygen atoms in the middle of the K-channel analogue	S6
Table S1: Protonation states of the histidines at pH=7 in CcO	S7
Table S2: Geometry-optimized coordinates and atomic charges for the BNC cofactors	S8
References	S12

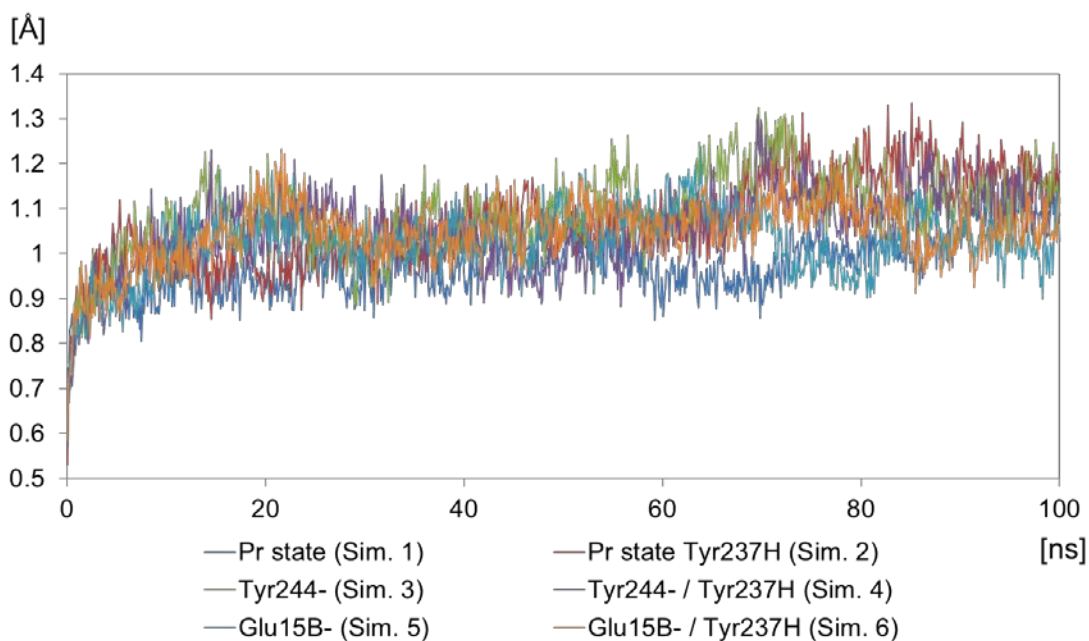


**Figure S1: Root mean square deviation (RMSD) of CcO backbone atoms** relative to the crystal structure PDB-id 3S8F [2] obtained by MD simulations for all simulations performed (for simulation details see Table I in main manuscript).

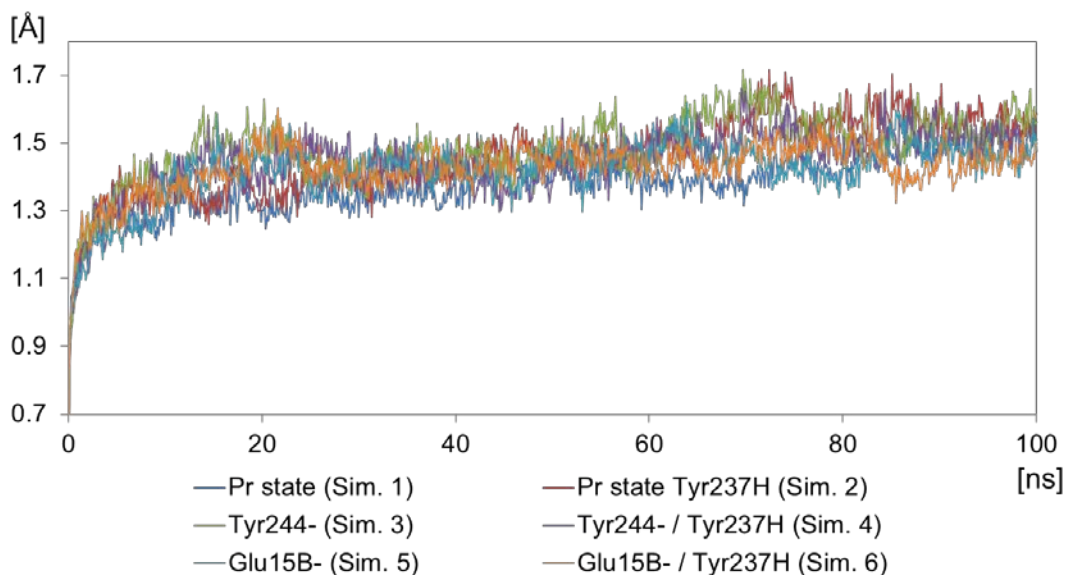


**Figure S2: Root mean square deviation (RMSD) of CcO of all protein atoms** relative to the crystal structure PDB-id 3S8F [2] obtained by MD simulations for all simulations performed (for simulation details see Table I in main manuscript).

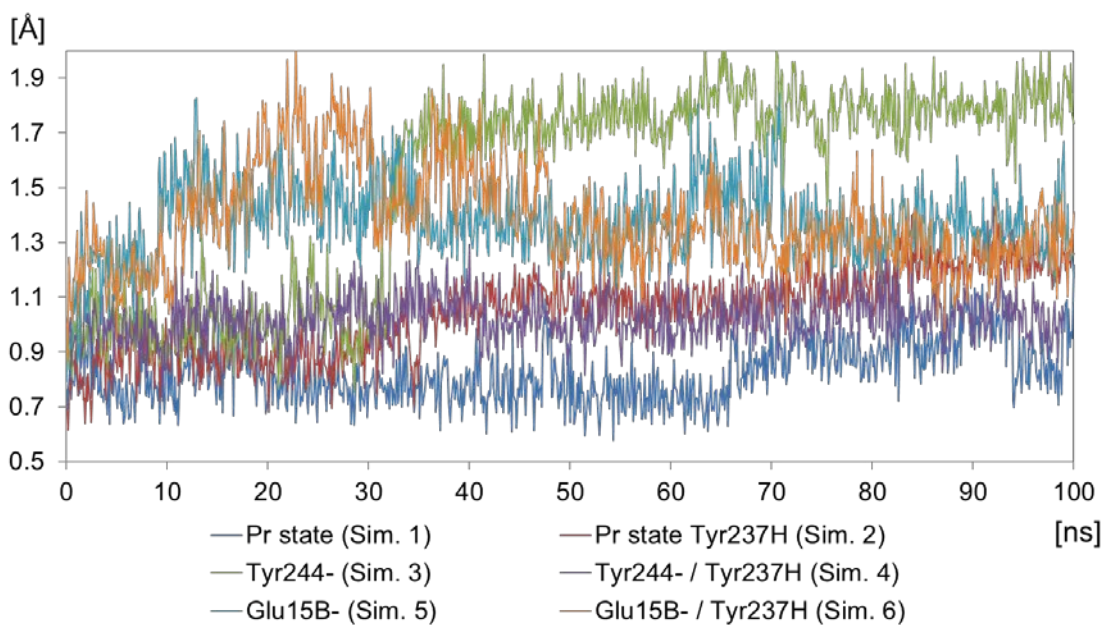


**Figure S3: Root mean square deviation (RMSD) of CcO of K-channel analogue residues.** MD simulation frames were aligned on the backbone atoms of the crystal structure (PDB-id 3S8F [2]). Then, RMSDs were measured for all atoms of the K-channel analogue residues (Tyr237, Ser309, Tyr244, Thr312, Tyr248, Thr315, Glu15B).

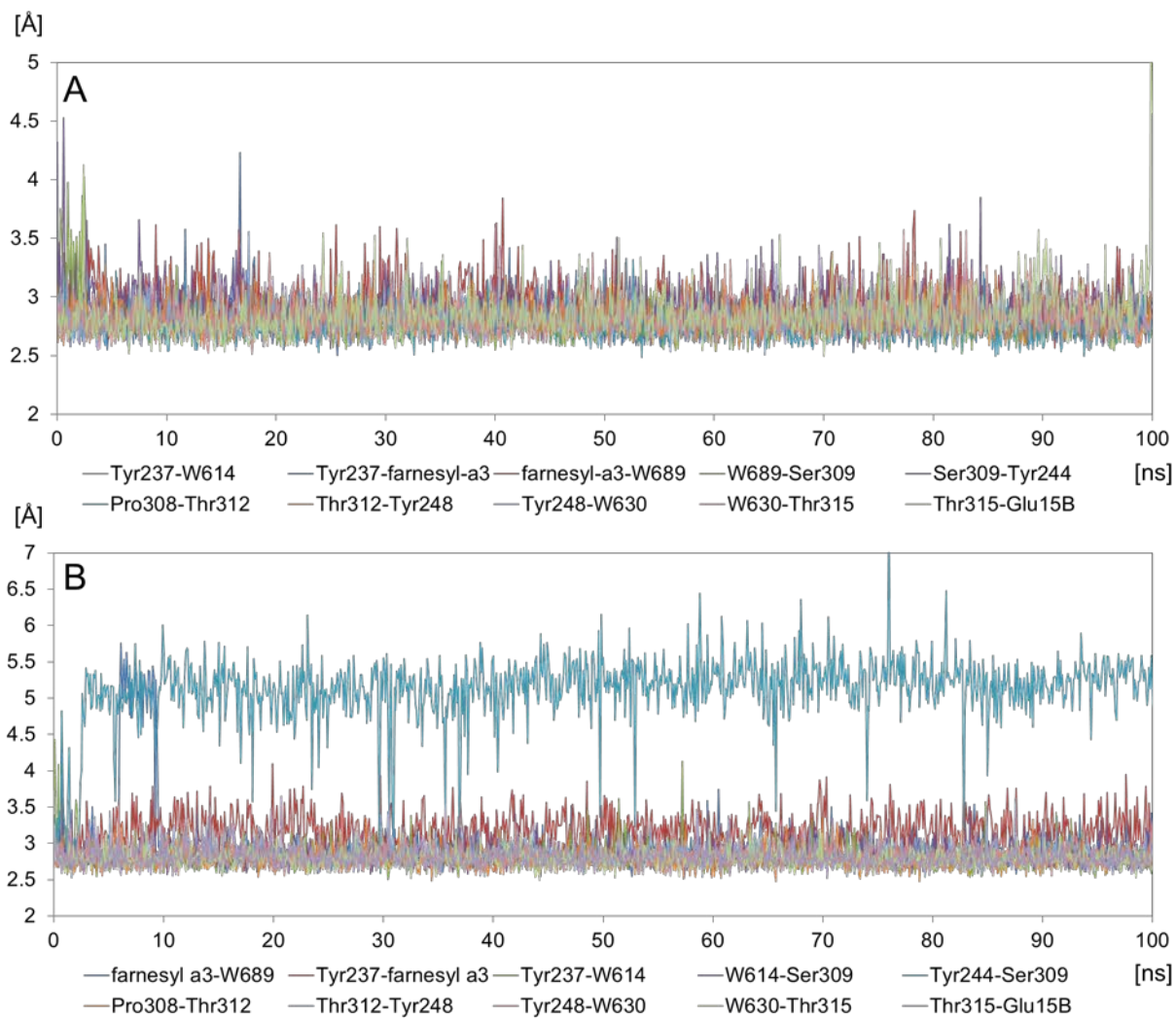


**Figure S4: Hydrogen-bonding distances between polar oxygen atoms in the K-channel analogue.** Distances between oxygen atoms were recorded for the 100 ns MD trajectory in (A)  $P_R$  state and (B) with Tyr237H (for simulation details see Table I, no. 1+2 in main manuscript).

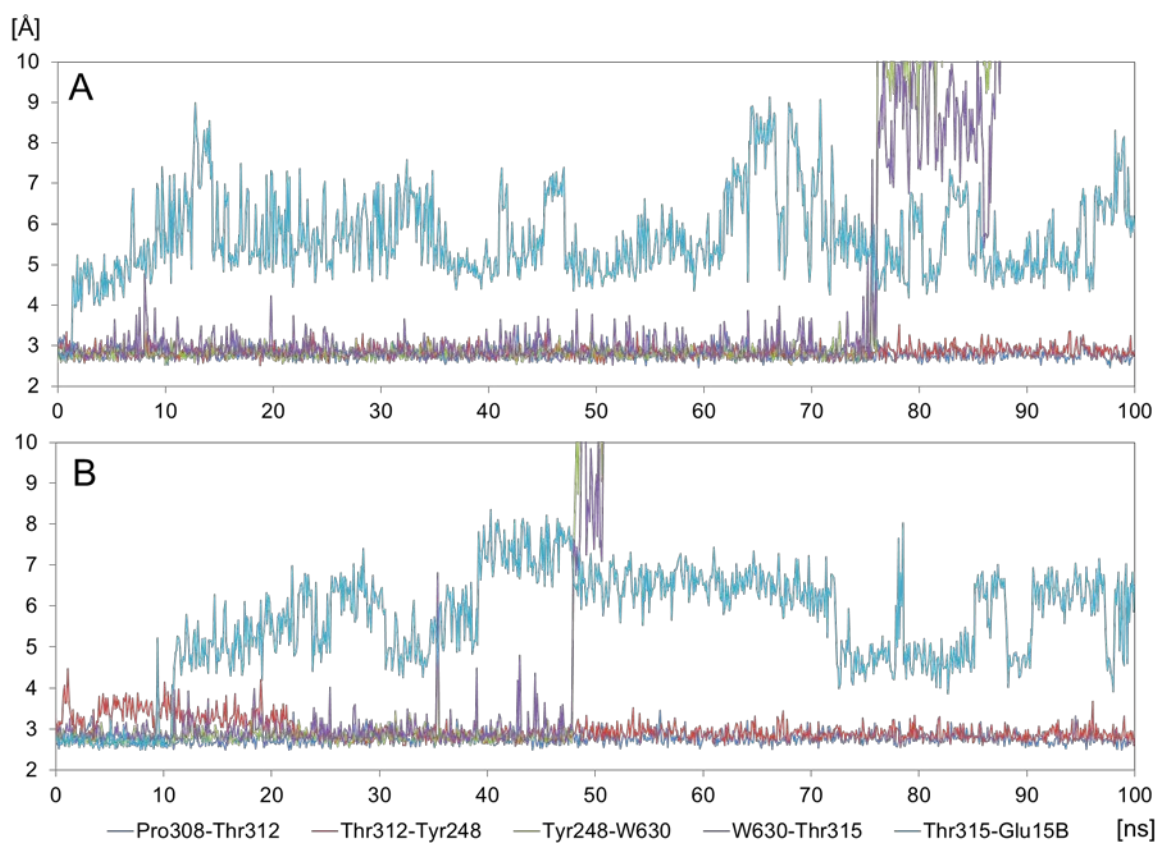


**Figure S5: Hydrogen-bonding distances between polar oxygen atoms at the entrance of the K-channel analogue.** Distances between oxygen atoms were recorded for the 100 ns MD trajectory with deprotonated Glu15B in (A)  $P_R$  state and (B) with Tyr237H (for simulation details see Table I, no. 5+6 in main manuscript).

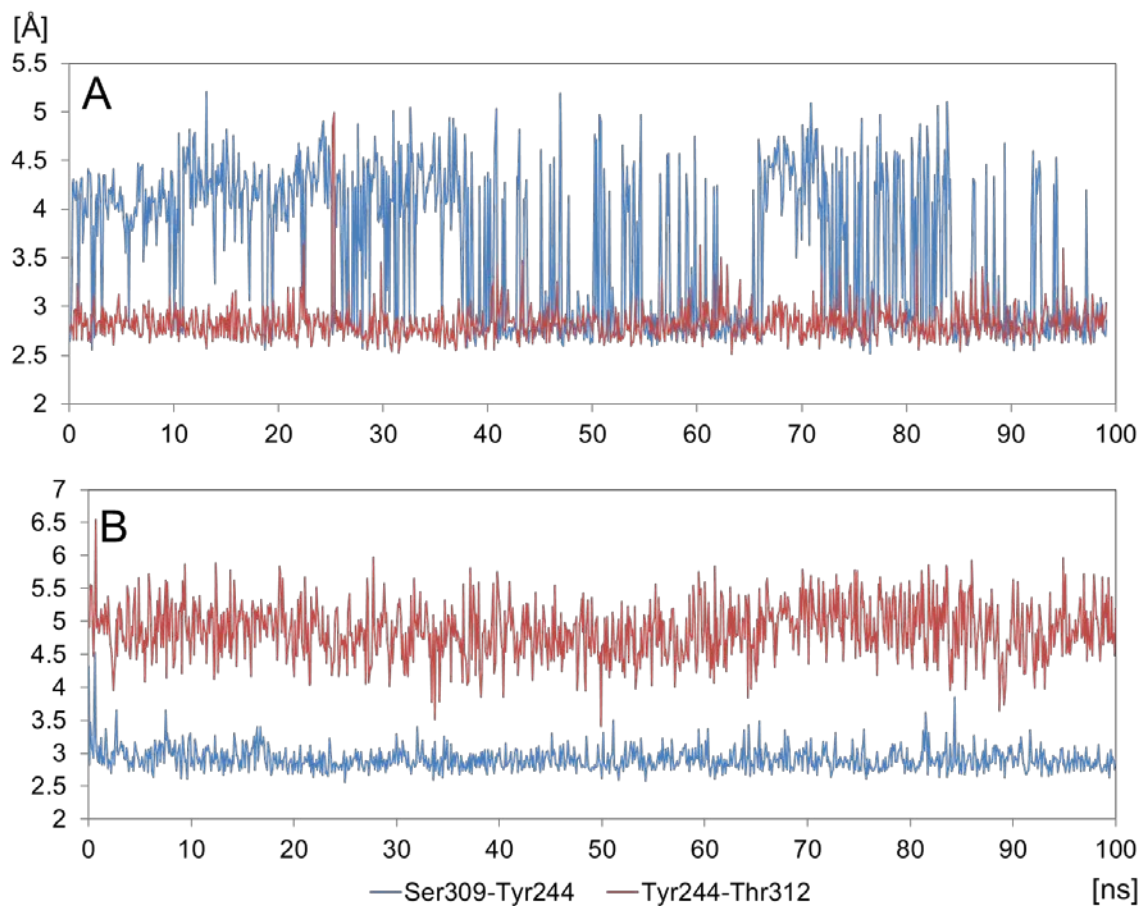
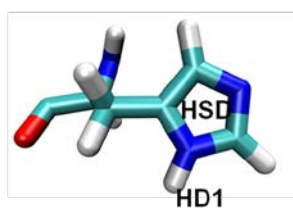
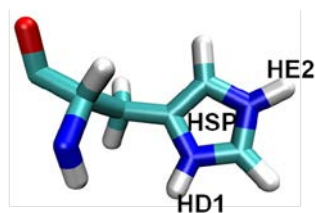
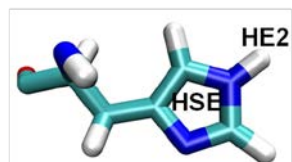


**Figure S6: Hydrogen-bonding distances between polar oxygen atoms in the middle of the K-channel analogue.** Distances between oxygen atoms were recorded for the 100 ns MD trajectory with (A) deprotonated Tyr244 and protonated Tyr237 and (B) in P<sub>R</sub> state (for simulation details see Table I, no. 3+1 in main manuscript).

**Table S1: Protonation states of the histidines at pH=7 in CcO (PDB-id 2GSM).**



The different protonation states of histidine are called HSP, HSD and HSE in the CHARMM[1] program.



AA	72 (A)	142 (A)	233 (A)	282 (A)	283 (A)	298 (A)	376 (A)	384 (A)	386 (A)
HisType	HSD	HSE	HSE	HSD	HSD	HSE	HSP	HSD	HSD
440 (A)	462 (A)	552 (A)	5 (B)	8 (B)	40 (B)	114 (B)	117 (B)	157 (B)	
HSD	HSE	HSD	HSE	HSD	HSE	HSE	HSE	HSE	

**Table S2: Geometry-optimized coordinates and atomic charges for the BNC cofactors.****a) CuA in oxidized state (used for all calculations)**

Cu1	-30.3270214596	148.9184511061	13.7615419482	0.311997
Cu2	-28.4194902574	147.0332691630	14.5574729498	0.311997
H3	-25.2084464886	148.7142486770	14.3672519247	0.132877
N4	-26.4180447344	147.0350061074	13.7613730923	-0.213947
C5	-25.2792104960	147.8039855783	13.7948458658	0.024317
C6	-26.3104004498	145.9874156863	13.0149433953	0.097385
H7	-27.0472576587	145.2276439342	12.8076710978	0.104494
N8	-25.0273624388	146.0202440434	12.5116533800	-0.193361
C9	-24.3662249887	147.1531184579	12.9921076707	-0.208905
H10	-23.3478442625	147.3702223383	12.7093699160	0.196572
C11	-30.6264341984	149.2368093769	16.9497028022	-0.005121
H12	-30.4054167205	148.7254743565	17.8889034834	0.051160
H13	-31.5650897477	148.8611676073	16.5406165089	0.051160
S14	-29.2290393107	148.9763774079	15.7792855141	-0.310848
N15	-29.0538688961	152.3462818304	14.3272468683	-0.905063
H16	-29.1249085687	151.3658659433	14.5726316043	0.331005
C17	-28.6592991126	152.5455030526	12.9512767613	0.210796
H18	-28.7145301876	153.6090198907	12.6975313624	0.052321
H19	-27.6134786516	152.2410036342	12.8189304878	0.028775
C20	-29.5141552252	151.6904314385	11.9991776517	0.415545
O21	-29.5435779802	150.4575644807	12.1093223297	-0.425493
N22	-30.4223645331	152.3424376739	11.2262762183	-0.713060
H23	-30.3115998988	153.3212532065	11.0056001449	0.340823
H24	-30.9970633615	151.7859976103	10.6064085380	0.378953
C25	-28.7727473311	147.3833845238	11.2819231234	0.101646
H26	-28.3851671725	146.5076054906	10.7559089054	0.022120
H27	-27.9553689119	148.0159583505	11.6245714914	0.022120
S28	-29.8141884519	146.8154649626	12.6947431327	-0.352773
H29	-33.2808170799	147.8994134365	12.8801623517	0.131131
N30	-32.2897306953	149.6188265009	13.7066361207	-0.147998
C31	-33.3333857278	148.9529431160	13.1069528429	-0.031274
C32	-32.6434209137	150.9186094890	13.8600279503	-0.018683
H33	-31.9863883607	151.7192103060	14.1609385453	0.133179
N34	-33.8670035199	151.0708698156	13.3622134927	-0.158875
C35	-34.3319449733	149.8509296044	12.8869753737	-0.154431
H36	-35.3179097335	149.7535293719	12.4594951925	0.177053
C37	-28.8008645918	144.5433665465	17.5359531210	-0.094367
H38	-29.8338392323	144.8572342928	17.3734838364	0.092250
H39	-28.5264599668	144.7327389645	18.5758743440	0.092250
S40	-27.7683885608	145.5455451624	16.4155875678	-0.220580
C41	-26.0783119079	145.0085812476	16.8369832484	-0.222799
H42	-25.4015144887	145.6254723219	16.2425678160	0.123502
H43	-25.8812513278	145.1873340764	17.8960677150	0.123502
H44	-25.9205965198	143.9567008975	16.5879251985	0.123502
H45	-24.6123510469	145.3410336601	11.8886099439	0.319269
H46	-34.4022407918	151.9283429563	13.3556921216	0.320702
H47	-29.7656802426	152.9419634016	14.7208235833	0.389642
H48	-30.6985977966	150.3070776053	17.1522811330	0.051160
H49	-29.3996092214	147.9516399790	10.5936179505	0.022120
H50	-28.7102417113	143.4791274433	17.3070069628	0.092250

**b) heme a in oxidized state (used for all calculations)**

H1	1.0239320577	-1.3183000967	38.9398941612	0.181210
C2	1.4909700298	-2.1324224093	38.4082267686	-0.126252
N3	2.4668918501	-2.9237006327	39.0000844501	-0.204047
C4	1.2861378809	-2.6540293935	37.1656361891	-0.136193
C5	2.8746383679	-3.8623337411	38.1188188228	-0.004414
N6	2.1887508740	-3.7038229060	37.0079671504	0.023538
H7	3.3010617514	-7.6716097547	31.0262020711	0.183593
C8	2.8189386081	-7.0847620378	31.7920567270	-0.118088
N9	1.4768473618	-6.7487184046	31.7139378525	-0.212660
C10	3.2757388779	-6.5531276053	32.9675072483	-0.203911
C11	1.1211226057	-6.0245334916	32.7849481888	-0.007644
N12	2.1757196738	-5.8833510427	33.5439998740	0.091744
C13	-1.2033153115	-3.8952969679	34.7482843924	-0.333782
C14	1.0683498935	-7.7360338829	36.8568703076	-0.215239
C15	5.5237873650	-5.7221106855	36.2039619395	-0.212895



C16 3.2880141988 -2.3070323447 33.4493402981 -0.167627  
 C17 -0.8764851168 -5.1961099437 35.3457753388 0.199004  
 C18 -1.8233223516 -6.2856272242 35.4378607023 -0.327948  
 C19 -1.2429350809 -7.2886238244 36.0795785368 0.222301  
 C20 0.1202440891 -6.9210944822 36.2681782075 0.065534  
 C21 -1.8264598055 -8.6265806947 36.4280023243 -0.360348  
 H22 -2.8629855560 -6.2001035017 35.1433657427 0.178094  
 C23 2.4403890906 -7.4095341963 36.9145825438 0.122940  
 C24 3.4545716847 -8.2428732404 37.5502690519 0.057027  
 C25 4.6855252720 -7.6285874638 37.4710702589 -0.005936  
 C26 4.4177819827 -6.4252747661 36.6297624112 0.096625  
 C27 3.1206281311 -9.4520075595 38.3799785215 -0.295983  
 C28 5.9908924779 -8.0940867938 37.9343020613 -0.101349  
 C29 6.2508615605 -8.6390349075 39.1317923800 -0.319434  
 C30 5.2927391525 -4.6809894736 35.1270879572 0.028820  
 C31 6.1902587286 -3.7680275644 34.8045987395 0.102032  
 C32 5.6135142001 -2.9276240257 33.7719798447 0.054588  
 C33 4.2854766480 -3.1099013493 34.0684863600 0.039909  
 C34 7.6814172627 -3.9478418006 34.9632157130 -0.302515  
 C35 6.1880366110 -1.8085038431 33.0423748568 -0.137651  
 C36 7.4852979481 -1.5995773340 32.7586685527 -0.301693  
 C37 1.9841093651 -2.4706336464 33.6606378982 0.134036  
 C38 0.9696371805 -1.4641848169 33.2148692074 0.086746  
 C39 -0.2914101054 -1.9201908563 33.6367409301 -0.324167  
 C40 -0.0831411170 -3.1818975699 34.2985367627 0.238467  
 C41 1.2140368575 -0.3478005172 32.2433300212 -0.292696  
 H42 -1.2466043426 -1.4523509067 33.4352140027 0.176273  
 N43 0.4488573285 -5.6781516584 35.6588858845 -0.276989  
 N44 3.0986426869 -6.3168742427 36.4000216410 -0.276989  
 N45 3.9187898095 -4.2543203730 34.8720651383 -0.276989  
 N46 1.2361344097 -3.3832150463 34.2856998002 -0.276989  
 Fe47 2.1751087947 -4.8471192658 35.3013198502 0.425000  
 H48 3.6397265093 -4.5970138349 38.3053640219 0.165195  
 H49 0.6146164615 -2.3374821273 36.3912458139 0.159761  
 H50 2.8430697625 -2.7919136913 39.9280966895 0.328887  
 H51 4.2467451855 -6.5573114858 33.4300010250 0.208630  
 H52 0.1355122674 -5.6284978918 32.9649365663 0.154493  
 H53 0.8633838827 -7.0028468966 30.9525158105 0.331262  
 H54 0.7600638035 -8.6704523913 37.3064450892 0.149311  
 H55 3.5870562216 -1.4559726303 32.8553294127 0.123769  
 H56 6.5144645763 -5.9699224250 36.5474862973 0.159482  
 H57 -2.2148318142 -3.5576469344 34.5826922848 0.198560  
 H58 7.7878610479 -0.7104617433 32.2147749139 0.147502  
 H59 8.2731175650 -2.2929914264 33.0225151671 0.159937  
 H60 5.4857200706 -1.0615661919 32.6816602697 0.140246  
 H61 7.2570469372 -8.9496295613 39.3957844083 0.151779  
 H62 5.4862963802 -8.7680336755 39.8914043546 0.161680  
 H63 6.8266151829 -7.9505769088 37.2503030047 0.123733  
 H64 4.0100335071 -10.0638624727 38.5495863659 0.098044  
 H65 2.7327612910 -9.1636237884 39.3650748215 0.098044  
 H66 2.3689667545 -10.0915887293 37.9047498233 0.098044  
 H67 8.1660145356 -2.9956206190 35.2032700204 0.100690  
 H68 7.9384912620 -4.6471427722 35.7621634222 0.100690  
 H69 8.1319283170 -4.3239521776 34.0382515860 0.100690  
 H70 -1.7381775272 -8.8385647174 37.4993707519 0.116140  
 H71 -2.8878358844 -8.6613100376 36.1705969314 0.116140  
 H72 -1.3216482278 -9.4381362872 35.8919764633 0.116140  
 H73 0.3003409076 0.2268552205 32.0703620493 0.101366  
 H74 1.9848331649 0.3546700968 32.5842350113 0.101366  
 H75 1.5444352287 -0.7431634898 31.2747706025 0.101366

**c) heme a3 in state Fe(IV)=O (used for all calculations)**

H38 -5.6190862081 -37.1675029949 20.5613171826 0.157824  
 N39 -6.8442915675 -36.1095730724 21.9895348831 -0.207126  
 H40 -7.6268375641 -36.7394697787 22.0790002153 0.316613  
 C41 -5.7335756117 -36.2909980218 21.1794846745 -0.138747  
 C42 -6.7010807601 -34.9238803102 22.6259582968 0.126215  
 H43 -7.4049957889 -34.5116211504 23.3320808668 0.105198  
 N44 -5.5503090507 -34.3588445223 22.2633277446 -0.335061  
 C45 -4.9452440472 -35.1883148349 21.3642905634 0.009826  
 H46 -3.9944289009 -34.9449101126 20.9190309940 0.086811  
 H47 0.2104785816 -34.9125771942 23.4328657543 0.160168

Fe48 -4.5184204499 -32.6416521663 22.8989580956 0.562061  
 N49 -2.8648006690 -33.7281769651 23.5761712994 -0.176399  
 N50 -5.3538540863 -32.7407635446 24.8568666373 -0.150605  
 N51 -5.9981861510 -31.3041549976 22.3726331576 -0.128398  
 N52 -3.5098871971 -32.2565793661 21.1056674638 -0.143865  
 C53 -1.7169820310 -33.9358358875 22.8478186742 0.206583  
 C54 -0.7880789194 -34.5975744229 23.7155774277 -0.290598  
 C55 -1.3746727485 -34.7646064123 24.9451906915 -0.063552  
 C56 -2.6944957702 -34.2251146125 24.8564708510 0.141559  
 C57 -4.8681833255 -33.5332831366 25.8795556988 0.067069  
 C58 -5.8658039558 -33.5129892003 26.9273318970 0.103347  
 C59 -6.9007876164 -32.7165331703 26.5310038895 -0.244257  
 C60 -6.5700017633 -32.2272437564 25.1999903716 0.123513  
 C61 -7.0682504703 -30.9200853988 23.1543873432 -0.017331  
 C62 -7.8484796438 -29.9605157689 22.4099332908 0.121088  
 C63 -7.2568045052 -29.7793826608 21.2031439710 -0.017751  
 C64 -6.0791782061 -30.6262827956 21.1599354178 0.044192  
 C65 -3.9463843793 -31.4023295552 20.1319859056 0.040356  
 C66 -2.9222565032 -31.3503961606 19.1140617013 0.167079  
 C67 -1.8971720724 -32.1559626221 19.5033762582 -0.385701  
 C68 -2.2764200639 -32.7262818211 20.7697046249 0.232631  
 C69 -1.5084520632 -33.5986734494 21.5199937226 -0.272957  
 H70 -0.5642673621 -33.9143238441 21.0845843150 0.140189  
 C71 -3.6557684319 -34.2007007233 25.8690995714 -0.212156  
 H72 -3.3668655714 -34.7215607305 26.7754817657 0.154845  
 C73 -7.3508851258 -31.3797296227 24.4232413008 -0.170412  
 H74 -8.2513585223 -31.0123450454 24.8996544773 0.158541  
 C75 -5.1727804438 -30.7339681631 20.1287022193 -0.173241  
 H76 -5.3804094412 -30.1468408745 19.2396427284 0.123366  
 C77 -0.7203503779 -35.3821699896 26.0968366526 0.401299  
 H78 0.2265947671 -35.9117239622 25.8461089048 -0.020246  
 O79 -1.1043938401 -35.3280839796 27.2558809620 -0.434365  
 C80 -5.7514258601 -34.2579373433 28.2295129919 -0.317330  
 H81 -4.7245613363 -34.5749254799 28.4271077037 0.104881  
 H82 -6.3742225561 -35.1614413140 28.2337424518 0.078587  
 H83 -6.0742325566 -33.6439578606 29.0778891479 0.111725  
 C84 -9.0845923040 -29.2873417000 22.9300720215 -0.278931  
 H85 -9.1282162297 -28.2434647254 22.6031701617 0.098724  
 H86 -9.1166819348 -29.2956137384 24.0230636382 0.077371  
 H87 -9.9993755422 -29.7844369728 22.5824207187 0.082733  
 C88 -7.6499638239 -28.9027824467 20.1007983288 -0.083917  
 H89 -6.8378605767 -28.5861745273 19.4469330884 0.121726  
 C90 -8.8730359307 -28.4174290989 19.8345425230 -0.378785  
 H91 -9.0308815006 -27.7465306164 18.9954392673 0.146703  
 H92 -9.7565007008 -28.7127535234 20.3888194855 0.158767  
 C93 -2.9973778799 -30.5271309401 17.8598757756 -0.300927  
 H94 -3.0532303148 -29.4538695223 18.0792403279 0.095647  
 H95 -3.8803334318 -30.7804087529 17.2598835186 0.078603  
 H96 -2.1151961718 -30.6908857339 17.2343759044 0.097210  
 C97 -8.0998014255 -32.3290711967 27.3565826724 0.319502  
 H98 -7.9081735958 -32.5670307831 28.4131962024 -0.016557  
 O99 -8.4723804561 -30.9546555075 27.2234886252 -0.613663  
 H100 -7.6842528621 -30.4249545479 27.4062866800 0.391412  
 H101 -8.9966290949 -32.8820456318 27.0496103428 0.034867  
 H102 -0.9698969828 -32.3452916349 18.9777700864 0.176710  
 O104 -3.7173545313 -31.3470686937 23.4935894406 -0.352657

**d) CuB in PR state with Cu(II)-OH Tyr237-O- (used for Tyr237 deprotonated)**

H1 -0.8264348977 -26.9346109600 26.1064242774 0.114395  
 N2 -2.2615098291 -28.5572664326 25.9604539222 -0.272336  
 C3 -1.8463080878 -27.2596556179 26.2418658027 -0.150851  
 C4 -3.5420971306 -28.6758556889 26.2606412562 0.239017  
 H5 -4.2047558321 -29.5248796211 26.1757183499 0.073658  
 N6 -4.0075359556 -27.4746763060 26.6779303239 0.018397  
 C7 -2.9594099957 -26.5594534038 26.6421526776 -0.139733  
 H8 -3.0851688944 -25.5565598424 27.0152909734 0.104747  
 H9 -7.4669767381 -24.5607221949 25.8510568872 0.096415  
 C10 -7.1688404465 -25.5584168702 26.1647318218 -0.355662  
 C11 -8.1455072571 -26.5516344439 26.3458615786 -0.025632  
 H12 -9.1974766433 -26.3140259532 26.2026918731 0.065093  
 C13 -7.7482593517 -27.8206578078 26.7208140444 -0.352689

H14 -8.4567905795 -28.6277836644 26.8823833952 0.101035  
 C15 -6.3642335389 -28.1607556020 26.8967965953 0.468574  
 O16 -5.9999644106 -29.3344808020 27.2440125686 -0.663003  
 C17 -5.8139427879 -25.8303667570 26.3081465185 -0.047149  
 H18 -5.0892850961 -25.0611900854 26.0485474013 0.091091  
 C19 -5.3883832049 -27.1014775020 26.7276621459 -0.156292  
 H20 0.7852770016 -33.3204222733 28.4027251972 0.151168  
 N21 -0.7357574042 -31.8060817970 28.5174237514 -0.138017  
 H22 -0.9905625006 -31.8829941978 29.4918222852 0.276540  
 C23 0.2228504796 -32.5635976410 27.8780136765 -0.274163  
 C24 -1.3050648697 -30.9706270807 27.6300361874 0.122950  
 H25 -2.0769605107 -30.2493471192 27.8480220333 0.070911  
 N26 -0.7548904222 -31.1951466430 26.4312355829 -0.347171  
 C27 0.2014882313 -32.1910163383 26.5710586696 0.066167  
 H28 0.7862817376 -32.5415473094 25.7365729296 0.093837  
 H29 3.7200734096 -31.2644666827 23.6833759693 0.099653  
 N30 1.9002902498 -31.5525148359 22.5596236380 -0.247127  
 H31 2.2419632600 -32.1739304486 21.8404850570 0.274181  
 C32 2.6731337940 -31.0195297081 23.5882368589 -0.084616  
 C33 0.6629101046 -31.0570231261 22.6444618907 0.048863  
 H34 -0.1651386774 -31.2846729282 21.9914555394 0.153108  
 N35 0.6137614190 -30.2121193382 23.6871710819 -0.100284  
 C36 1.8581144913 -30.1821177181 24.2830129771 -0.176187  
 H37 2.0642151958 -29.5799968425 25.1542071162 0.134585  
 Cu103 -1.0845506669 -29.8341269628 24.8938509096 0.345165  
 O106 -1.7536237560 -29.0975303164 23.2951111386 -1.015467  
 H107 -2.0035987608 -28.1759530489 23.4461681401 0.336828

**e) CuB in PR state with Cu(II)-OH Tyr237-OH (used for Tyr237 protonated)**

H1 -0.8903030011 -26.9122738263 26.1209729916 0.163635  
 N2 -2.2944940036 -28.5611061666 25.9699135968 -0.278232  
 C3 -1.9042401272 -27.2567284765 26.2489171452 -0.090344  
 C4 -3.5629998273 -28.7017951339 26.2571793843 0.114349  
 H5 -4.1555995250 -29.5928522102 26.1474667632 0.102382  
 N6 -4.0697007471 -27.5087776324 26.6699145053 0.115890  
 C7 -3.0311687802 -26.5748483892 26.6373482137 -0.178669  
 H8 -3.1643250919 -25.5708792226 27.0043431557 0.178374  
 H9 -7.4289088137 -24.4878232579 25.8404578774 0.143010  
 C10 -7.1677891328 -25.4920844851 26.1555426415 -0.156157  
 C11 -8.1532012886 -26.4580572992 26.3452393144 -0.046268  
 H12 -9.2010846602 -26.2104477308 26.2097203661 0.132988  
 C13 -7.7974924142 -27.7498716023 26.7265000525 -0.251665  
 H14 -8.5623231913 -28.5071009605 26.8828991695 0.148767  
 C15 -6.4586858996 -28.1008086512 26.8894203036 0.255685  
 O16 -6.0817660469 -29.3642035986 27.2643312960 -0.514649  
 C17 -5.8258681756 -25.8433330865 26.3050153643 -0.130014  
 H18 -5.0605022373 -25.1208508519 26.0473666949 0.142600  
 C19 -5.4570884075 -27.1219376779 26.7247512580 0.007477  
 H20 0.8816957634 -33.3136059777 28.3882102465 0.182608  
 N21 -0.6722779252 -31.8329388865 28.5058845328 -0.159156  
 H22 -0.9231420263 -31.9243597913 29.4806466206 0.319914  
 C23 0.3037379213 -32.5667058229 27.8661568171 -0.148849  
 C24 -1.2572878384 -31.0061882653 27.6199517629 0.065660  
 H25 -2.0434563230 -30.3068276519 27.8476507982 0.128051  
 N26 -0.6989880281 -31.2141920885 26.4215024389 -0.275759  
 C27 0.2781578347 -32.1892493218 26.5585397689 -0.003117  
 H28 0.8732574990 -32.5246893992 25.7253295240 0.111948  
 H29 3.7403608534 -31.2684578974 23.6634306582 0.154390  
 N30 1.9002898232 -31.5594265318 22.5739080537 -0.191458  
 H31 2.2255561008 -32.1901799057 21.8541887948 0.316181  
 C32 2.6929735597 -31.0204729792 23.5826282592 -0.074571  
 C33 0.6673097257 -31.0564169619 22.6763088870 0.081909  
 H34 -0.1710067264 -31.2888561002 22.0381824965 0.176658  
 N35 0.6401165951 -30.2000763563 23.7120840579 -0.220788  
 C36 1.8964372889 -30.1715901007 24.2847790246 -0.096136  
 H37 2.1260542437 -29.5638892556 25.1459890337 0.152475  
 Cu103 -1.0521976077 -29.8551141939 24.8881634956 0.593722  
 O106 -1.7456079573 -29.1113523064 23.3121095522 -0.760961  
 H107 -2.0223354844 -28.1942349722 23.4410356975 0.367948  
 H41 -6.8166525527 -29.9729106423 27.1083927072 0.420178

## References

1. Brooks, B.R., et al., *CHARMM: A Program for Macromolecular Energy, Minimization, and Dynamics Calculations*. J. Comput. Chem., 1983. **4**(2): p. 187-217.
2. Tiefenbrunn, T., et al., *High Resolution Structure of the ba3 Cytochrome c Oxidase from Thermus thermophilus in a Lipidic Environment*. PLoS One, 2011. **6**(7): p. e22348.